JBIC Journal of Biological Inorganic Chemistry (2024) 29:279–290
https://doi.org/10.1007/s00775-024-02056-y

ORIGINAL PAPER

Revisiting the metal sites of nitrous oxide reductase in a low-dose structure from *Marinobacter nauticus*

Anja Pomowski[1] · Simone Dell'Acqua[2] · Anja Wüst[1] · Sofia R. Pauleta[3,4] · Isabel Moura[5] · Oliver Einsle[1]

Received: 28 January 2024 / Accepted: 10 April 2024 / Published online: 8 May 2024

Abstract

Copper-containing nitrous oxide reductase catalyzes a 2-electron reduction of the green-house gas N_2O to yield N_2. It contains two metal centers, the binuclear electron transfer site Cu_A, and the unique, tetranuclear Cu_Z center that is the site of substrate binding. Different forms of the enzyme were described previously, representing variations in oxidation state and composition of the metal sites. Hypothesizing that many reported discrepancies in the structural data may be due to radiation damage during data collection, we determined the structure of anoxically isolated *Marinobacter nauticus* N_2OR from diffraction data obtained with low-intensity X-rays from an in-house rotating anode generator and an image plate detector. The data set was of exceptional quality and yielded a structure at 1.5 Å resolution in a new crystal form. The Cu_A site of the enzyme shows two distinct conformations with potential relevance for intramolecular electron transfer, and the Cu_Z cluster is present in a [4Cu:2S] configuration. In addition, the structure contains three additional types of ions, and an analysis of anomalous scattering contributions confirms them to be Ca^{2+}, K^+, and Cl^-. The uniformity of the present structure supports the hypothesis that many earlier analyses showed inhomogeneities due to radiation effects. Adding to the earlier description of the same enzyme with a [4Cu:S] Cu_Z site, a mechanistic model is presented, with a structurally flexible Cu_Z center that does not require the complete dissociation of a sulfide prior to N_2O binding.

Keywords Nitrogen cycle · Nitrous oxide · N_2O reductase · X-ray crystallography · Denitrification · Copper-containing enzyme

Abbreviations

N_2OR	Nitrous oxide reductase
EPR	Electron paramagnetic resonance
MR	Molecular replacement

✉ Oliver Einsle
einsle@biochemie.uni-freiburg.de

[1] Institute for Biochemistry, Albert-Ludwigs-University Freiburg, Albertstrasse 21, 79104 Freiburg, Germany

[2] Dipartimento Di Chimica, Università Di Pavia, Via Taramelli 12, 27100 Pavia, Italy

[3] Microbial Stress Lab, UCIBIO—Applied Molecular Biosciences Unit, Department of Chemistry, NOVA School of Science and Technology, Universidade NOVA de Lisboa, 2829-516 Caparica, Portugal

[4] Associate Laboratory i4HB—Institute for Health and Bioeconomy, NOVA School of Science and Technology, Universidade NOVA de Lisboa, 2829-516 Caparica, Portugal

[5] LAQV, Department of Chemistry, NOVA School of Science and Technology, Universidade NOVA de Lisboa, 2529-516 Caparica, Portugal

Introduction

Bacterial denitrification is the dominant respiratory metabolic pathway in many microoxic or anoxic environments [1]. Denitrifying microorganisms assemble an electron transport chain in the cytoplasmic membrane that couples the stepwise reduction of nitrate (NO_3^-) via nitrite (NO_2^-), nitric oxide (NO), and nitrous oxide (N_2O) to dinitrogen (N_2) to the generation of a proton motive force [2]. The final step of the pathway is a 2-electron reduction of N_2O catalyzed by the copper-containing enzyme nitrous oxide reductase (N_2OR) [3–5]. The process of fertilization in industrial agriculture creates nitrate-rich habitats that support the growth of denitrifying microbes to compete with crop plants, and N_2OR then often is inactivated and gaseous N_2O is released as a metabolic end product [6], resulting in a steady rise in atmospheric levels of nitrous oxide, in lockstep with the increasing fertilizer use during the past century [7]. With a global warming potential that exceeds the one of CO_2 300-fold, nitrous oxide is a potent green-house gas, and it has an additional deleterious effect as an ozone-depleting

substance. Its increasing concentration in the atmosphere has thus prompted its designation as the most critical anthropogenic emission in the twenty-first century [8].

Marinobacter nauticus, formerly known as *Pseudomonas nautica* or *Marinobacter hydrocarbonoclasticus* [9], is a denitrifying, marine Gammaproteobacterium that forms biofilms on hydrophobic organic matter but can also sustain a pelagic lifestyle [10]. Its N_2OR is a 130 kDa homodimer encoded by the *nosZ* gene that contains two copper sites, Cu_A and Cu_Z [11]. Cu_A, a dinuclear, mixed-valent [$Cu^{1.5+}$:$Cu^{1.5+}$] center, transfers a single electron with a midpoint redox potential of + 65 ± 5 mV, at pH 7.6 [12]. It is located in the C-terminal cupredoxin domain of NosZ, similar to the Cu_A site in cytochrome *c* oxidase [13]. The N-terminal domain of NosZ, with a 7-bladed β propeller fold, holds the Cu_Z center, a tetranuclear copper cluster that is unique to N_2OR. The enzyme from *M. nauticus* was the first to be characterized by X-ray crystallography, and an initial description of Cu_Z as a [4Cu:O] center [14] was subsequently revised to a [4Cu:S] stoichiometry [15], in line with available spectroscopic data [5, 16] and with further structural analyses of the enzymes from *Paracoccus denitrificans* [17] and "*Achromobacter cycloclastes*" [18]. In these structures, Cu_Z is a μ_4-S-bridged Cu cluster with a total charge of +3, i.e., formal copper oxidation states of [$1Cu^{2+}$:$3Cu^{+}$] [3]. This state is characterized by a single band at 650 nm in electron excitation spectroscopy, arising from an S → Cu LMCT transition resulting in a blue color of the enzyme [19]. This simple spectrum is commonly masked by the more complex signature of the mixed-valent Cu_A yielding a pink enzyme, but can be revealed when the binuclear site is reduced to a colorless all-cuprous state with ascorbate [20]. The pink form of N_2OR has been designated form II [5] and was obtained as the oxidized state of the enzyme when prepared in the presence of dioxygen [17, 18, 20]. A spectroscopically distinct, purple form I was first described for *Pseudomonas stutzeri* [21], but was later also found in *Achromobacter xylosoxidans* [22] and *M. nauticus* [23]. It shows an absorption maximum at 538 nm, and while it can also be reduced with ascorbate to a blue form, this resulting species consists of two bands at 552 nm and 650 nm and is thus distinct from the one described above [4]. In 2011, the purple N_2OR from *P. stutzeri* was crystallized under anoxic conditions [24], revealing that here the enzyme contains a Cu_Z site of composition [4Cu:2S] [25]. The second sulfur atom in this site, S_{Z2}, is labile and seems to be depleted—to varying degrees—in different batches of protein. This revised stoichiometry of the tetranuclear site explained the spectroscopic findings and clarified that the Cu_Z site of purple N_2OR form I is a [4Cu:2S] cluster, while the desulfurated [4Cu:S] cluster of the pink form II enzyme was assigned as the Cu_Z* species defined previously by spectroscopy [4, 5]. In purple N_2OR as isolated, Cu_Z is present in a [$2Cu^{2+}$:$2Cu^{+}$] state that cannot be reduced with ascorbate but converts to a [$1Cu^{2+}$:$3Cu^{+}$] state upon incubation with dithionite [3]. This state is distinct from the one found for Cu_Z* with respect to its EPR spectra. Based on a recombinant production system for active N_2OR in *E. coli* that yielded catalytically active, purple N_2OR with a [4Cu:2S] Cu_Z site [26], the systematic replacement of the seven histidine ligands to Cu_Z led to a complete loss of metalation in six cases, but to an unexpected spectrum resembling a form II enzyme in the case of the H382A variant [27]. However, rather than the [4Cu:2S] Cu_Z cluster commonly associated with this spectrum, the crystal structure of H382A N_2OR contained a [3Cu:2S] center that was catalytically inactive but retained three copper ions liganded by sulfides, and it still produced the CT band at 650 nm. Interestingly, sulfide S_{Z2} was present in this cluster, but in the absence of the Cu_{Z1} ion it bound in the native enzyme, it had shifted its position toward a nearby lysine. The implication was that the difference between the reported Cu_Z and Cu_Z* sites may not be the complete loss of sulfide S_{Z2} [28], but rather its dissociation from Cu_1 that also leads to the loss of the 552 nm CT band, rendering the second sulfide invisible in UV/Vis spectra. If so, this may reconcile different hypotheses about the mode of N_2O binding to the Cu_Z site and the mechanism of its reduction, as a mechanistic proposal for N_2OR had suggested substrate binding to Cu_1 and Cu_4 of Cu_Z [29–31], which seemed incompatible with the presence of S_{Z2}, but may well be feasible if the shift of S_{Z2} would render both Cu_1 and Cu_4 three-coordinate [27].

Considering these results, we revisited *M. nauticus* N_2OR, whose initial analysis had a [4Cu:S] Cu_Z site with H_2O bound at the Cu_1–Cu_4 edge (PDB 1QNI), providing the basis for the proposed mechanism [29]. The positive midpoint potential of copper sites in proteins makes them particularly prone to photoreduction or even more severe forms of radiation damage during diffraction data collection at high-flux X-ray sources, such as synchrotrons. We therefore analyzed the anoxically isolated, purple form of *Mn*N_2OR using the far lower photon flux of a rotating anode X-ray generator while retaining cryogenic conditions during data collection, aiming to generate a diffraction data set that was unperturbed by radiation-induced effects and more accurately represented the enzyme in its active form as isolated from its native host.

Experimental procedures

Cell growth and protein purification

M. nauticus was grown under denitrifying conditions in the presence of nitrate, as described elsewhere [16]. Cell disruption was carried out in an anoxic chamber with an

N_2/H_2 (95%/5%) atmosphere (Coy Labs), where H_2 was used to react with residual oxygen on a platinum catalyst surface to maintain $pO_2 < 1$ ppm. During protein purification, samples, buffers, and columns were kept anoxic using modified Schlenk techniques. Approximately 180 g of cells (wet weight) were resuspended in 10 mM Tris/HCl buffer at pH 7.6 and broken in a microfluidizer (microfluidics). From the resulting crude extract, cell debris and membranes were sedimented by centrifugation at 100,000×*g* for 1 h. With the supernatant, all steps were carried out without breaks to avoid storage of the sample or freeze–thaw cycles. The soluble fraction was loaded onto a DEAE-FF anion exchange column (GE Healthcare) equilibrated with 10 mM Tris/HCl buffer at pH 7.6 and washed with the same buffer until A_{280nm} reached baseline. The column was developed with a linear gradient from 10 to 500 mM Tris/HCl buffer, pH 7.6, from which N_2O reductase eluted at approximately 300 mM Tris/HCl. The pooled fractions of the elution peak were then dialyzed against 10 mM Tris/HCl buffer at pH 7.6, and subsequently loaded onto a second anion exchange column (HiTrapQ, GE Healthcare) that was equilibrate in the same buffer. The column was again washed to baseline and developed with a linear gradient from 10 to 500 mM Tris/HCl buffer, pH 7.6, with elution of N_2OR at approximately 300 mM Tris/HCl. As a final step, the eluate was loaded onto a Superdex 200 size exclusion column (Cytiva) equilibrated with 300 mM Tris/HCl buffer at pH 7.6. The pure enzyme eluted as a symmetric peak and was concentrated by ultrafiltration (50 kDa MWCO, Sartorius) to 14 mg mL^{-1}, while at the same time, the buffer was exchanged to 10 mM Tris/HCl, pH 7.6, for crystallization. Protein was determined using the bicinchoninic acid method [32], using bovine serum albumin as protein standard.

Crystallization and data collection

MnN_2OR was crystallized by sitting drop vapor diffusion in an anoxic glove box (Coy Labs) at 303 K, in an N_2/H_2 atmosphere with < 1 ppm O_2. 2 µL of protein solution (14 mg mL^{-1}) were mixed with 2 µL of a reservoir solution containing 15% (*w/v*) polyethylene glycol 8000, 0.6 M NaCl, and 0.1 M imidazole/malate buffer at pH 7.2 and equilibrated against 50 µL of the same reservoir solution in a sealed crystallization plate (SwissSci). Large plate-like crystals were obtained in less than 1 day. For data collection, a crystal was transferred into a harvesting buffer that consisted of the reservoir solution with 15% (*v/v*) of 2*R*,3*R*-butane diol as a cryoprotectant. The crystal was then flash-cooled in liquid nitrogen before being removed from the anoxic chamber. Diffraction data were collected on a rotating copper anode X-ray generator (Rigaku MicroMax 007HF with a marresearch mar345dtb image plate system) at a wavelength of λ = 1.5418 Å and a temperature of 100 K.

Structure solution and refinement

The data set was integrated with XDS [33] and scaled with AIMLESS [34] from the CCP4 suite [35]. Molecular replacement with MOLREP [36] was used to locate two copies of the dimeric enzyme in the asymmetric unit, using the previous structure of *Mn*N_2OR (PDB 1QNI) as a search model. Model building was conducted in COOT [37], and REFMAC5 [38] was used for refinement. The quality of the final model was evaluated with MolProbity [39]. Data collection and refinement statistics are summarized in Table 1.

Table 1 Data collection and refinement statistics

Data set	
Space group	*P* 1
Cell constants *a, b, c* [Å] *α, β, γ* [°]	65.2, 69.4, 153.1 81.4, 77.9, 88.6
Wavelength [Å]	1.5418
Resolution limits [Å]	23.49 – 1.50 (1.52 – 1.50)
Completeness (%)	91.4 (83.4)
Total number of observations	757,181 (33,806)
Unique reflections	381,570 (17,344)
Multiplicity	2.0 (1.9)
R_{merge} [a]	0.026 (0.258)
$R_{p.i.m}$ [62]	0.026 (0.258)
Mean I/σ(I)	12.1 (3.0)
$CC_{1/2}$ (outer shell) [63]	0.870
Refinement statistics	
R_{cryst} [b]	0.135 (0.294)
R_{free}	0.158 (0.322)
Non-hydrogen atoms excl. solvent	18,482
Solvent molecules	3,222
Cruickshank's DPI (Å) [64]	0.036
Wilson B-factor ($Å^2$)	45.6
Avg. B-factor protein ($Å^2$)	69.2
Avg. B-factor cofactors ($Å^2$)	59.0
Avg. B-factor solvent ($Å^2$)	56.2
r.m.s. deviations from ideal values	
Bond lengths (Å)	0.005
Bond angles (°)	1.10
Ramachandran statistics	
Preferred regions	2072 (93.8%)
Allowed regions	117 (5.3%)
Outliers	19 (0.9%)

[a] $R_{merge} = \Sigma_{hkl}\left[\left(\Sigma_i|I_i - I|\right)/\Sigma_i I_i\right]$

[b] $R_{cryst} = \Sigma_{hkl}\left||F_{obs}| - |F_{calc}|\right| / \Sigma_{hkl}|F_{obs}|$

R_{free} is the cross-validation *R* value for a test set of 5 % of unique reflections

[c] Ramachandran statistics as defined by PROCHECK [65]

Results and discussion

Diffraction data from a plate-like single crystal of *Mn*N_2OR were collected using Cu K_α radiation ($\lambda = 1.5418$ Å) on a rotating anode X-ray generator with a mar345dtb image plate detector at a temperature of 100 K. The crystal belonged to the triclinic space group *P*1 and diffracted beyond the detector edge at the minimal possible crystal-to-detector distance, yielding data to 1.5 Å resolution with a mean $I/\sigma(I)$ of 2.6 in the highest resolution shell (Table 1). The data set proved to be of outstanding quality and the excellent electron density map compared favorably to the best available data obtained from synchrotron sources, while presumably not suffering from radiation-induced changes in the architecture of the metal sites. Notably, the quality of the map also far exceeded that of the earlier, synchrotron-derived structure from the same organism that was refined to 2.4 Å resolution (PDB 1QNI) [14, 15]. This crystal form contained two N_2OR dimers in the asymmetric unit and thus four independent observations of each feature.

Overall structure

The low-dose structure of *Mn*N_2OR aligns with the previous model with a root-mean-squared deviation (r.m.s.d.) of 0.25 Å for 7727 atoms [14, 15]. The additional level of detail offered by the improved resolution allows for a detailed comparison with structures of the enzyme from other organisms. *Mn*N_2OR forms the typical head-to-tail homodimer (Fig. 1A), with the N-terminal, seven-bladed β-propeller domain of one monomer in close contact with the C-terminal cupredoxin domain of the other (Fig. 1B). At the interface of both domains, the Cu_A site closely approaches the Cu_Z cluster of the other subunit to form a combined active site that is accessible via a hydrophobic substrate channel running along the subunit interface, with a water-filled cavity behind the Cu_Z cluster (Fig. 1C). These features were previously observed in a structure of *Ps*N_2OR prepared under anoxic conditions after pressurization with N_2O gas, in which the substrate N_2O was bound between the two copper sites [25]. The gaseous substrate N_2O and product N_2 enter and exit via this hydrophobic channel, while the second product, H_2O, can exit through the water-filled cavity [4].

The electron transfer site Cu_A

Originally described as one of the two spectroscopically distinct copper sites in respiratory cytochrome *c* oxidase, the exact nature of Cu_A remained under debate ('embattled', in the words of Helmut Beinert) for years [40, 41]. In EPR, Cu_A appeared with an unusually small hyperfine splitting around $g_\perp = 2.18$ that in most cases was not even resolved into what was expected to be a four-line pattern for a mononuclear copper, and the presence of hemes *a* and a_3 in the oxidase further obfuscated the signature of the copper site. In 1989, Dooley and Zumft showed that *Ps*N_2OR also contains a Cu_A-type site that is not masked by the presence of heme, and after some exchange on the nature of Cu_A [42, 43], Kroneck, Zumft, and others established along various lines the dinuclear, valence-delocalized nature of the site even before a first crystal structure of cytochrome *c* oxidase became available [44, 45]. In structures of cytochrome *c* oxidases, N_2O reductases and diverse natural and engineered Cu_A domains [19, 46–48], two Cu ions form a central rhomb with the thiols of two cysteines, and the distorted tetrahedral ligand environment of the coppers is completed by a histidine at each metal, plus a methionine for Cu_{A1}, the ion more distal from the Cu_Z cluster (Fig. 2), and a backbone carbonyl for Cu_{A2}. The same arrangement was found and modeled in both Cu_A sites within the *Mn*N_2OR dimer (Fig. 2A, B), with C614 and C618 as bridging cysteines, H579 and M625 as ligands to Cu_{A1}, and H622 and the backbone carbonyl of W616 as ligands to Cu_{A2} (Fig. 2C). The initial analysis of *Mn*N_2OR had established these residues and modeled all six occurrences of Cu_A in the asymmetric unit in the same conformation [14]. This uniform nature of Cu_A was first challenged with the analysis of *Ps*N_2OR under anoxic conditions [25], where the corresponding Cu_A sites now attained two distinct conformations. Typically, in one of the two copies of the monomer, the histidine ligand to Cu_{A2} (H583 in this organism) had its imidazole moiety rotated away from Cu_{A1} by 130° to form a short hydrogen bond to a nearby serine (S550). In the following, this will be designated the OUT-conformation. Only in structures with bound N_2O, this histidine was consistently flipped back to the copper (the IN conformation), and we hypothesized at the time that this may represent a mechanism to gate electron transfer during catalysis [25]. Upon establishment of a recombinant production system for a functional *Ps*N_2OR in *E. coli*, [26] the metal-replete form I structure had both Cu_A sites in the OUT-conformation at Cu_{A1}. For the low-dose structure reported here, generated from protein isolated from actively denitrifying *M. nauticus*, the conformations of the Cu_A sites were therefore of particular interest.

The two N_2OR dimers of the asymmetric unit indeed differed in the conformation of residue H579, which was a ligand to Cu_{A1} in the A protomer of both dimers (IN conformation) (Fig, 2A, C), but rotated toward S546 in protomer B (OUT-conformation) (Fig. 2B, F). These positions corresponded to the two conformations observed in the first *Ps*N_2OR structures, and the precise definition of both sites now allowed to resolve distortions and asymmetries of the metal centers. In the IN conformation of protomer A, the Cu_2S_2 rhomb was already slightly

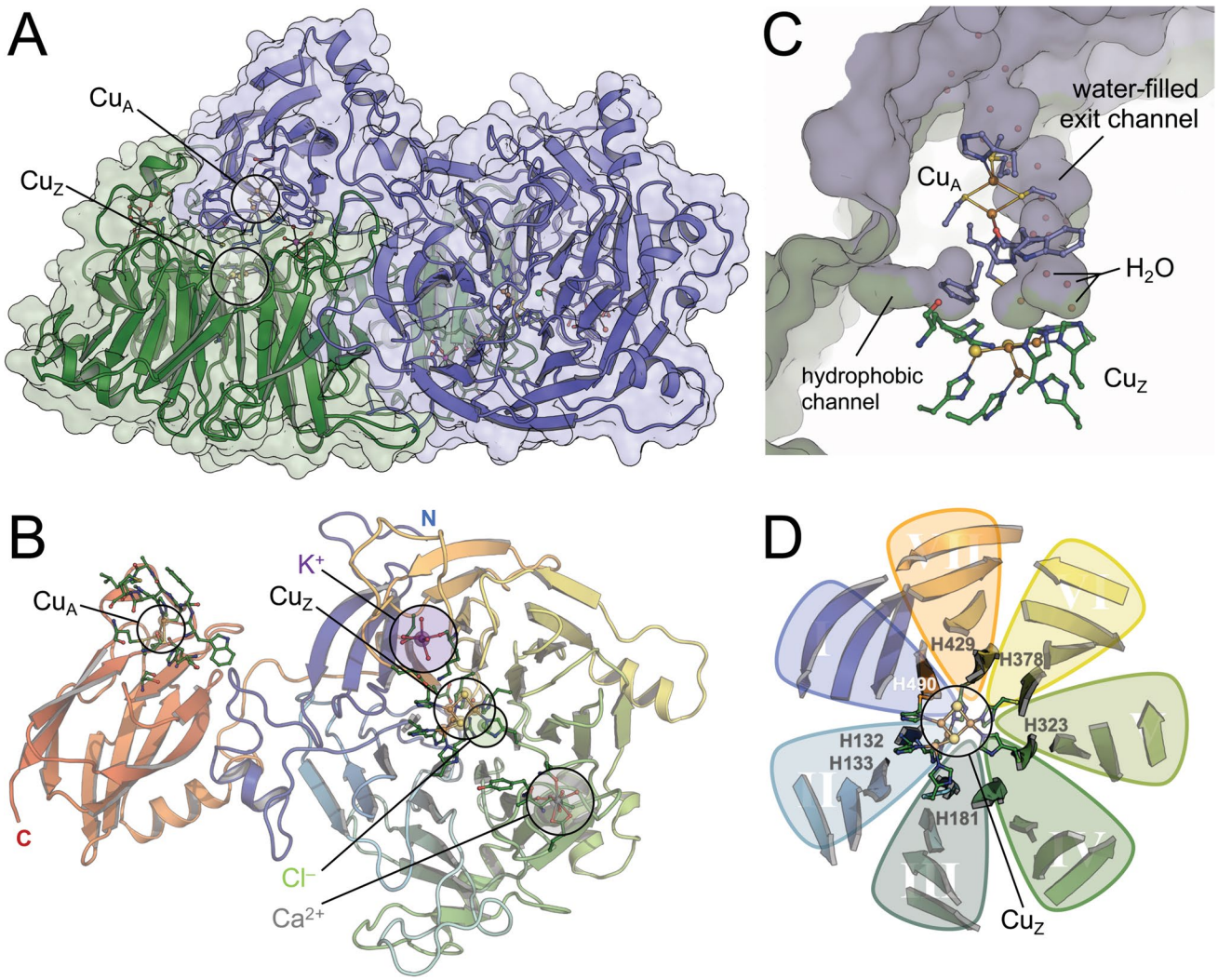

Fig. 1 Low-dose structure of *M. nauticus* N_2OR. **A** The head-to-tail homodimer of N_2OR with protomer A in green, protomer B in blue. The Cu_A site of one protomer forms a combined active site with the Cu_Z site of the other. **B** Cartoon representation of a NosZ monomer with the distinct two-domain architecture, colored from blue at the N-terminus to red at the C-terminus. The N-terminal domain forms a seven-bladed β-propeller with Cu_Z at its center, while Cu_A is bound to the C-terminal domain, which attains the cupredoxin fold. The positions of the ions discussed in the text are indicated. **C** A hydrophobic channel along the dimer interface allows for access of the substrate N_2O and egress of product N_2, while the second product water is released into a water-filled exit channel that leads back to the protein surface. **D** The seven blades of the N-terminal domain and Cu_Z at the hub of the propeller. Except for blade IV, each blade contributes a histidine ligand to Cu_Z. Blade II contributes two consecutive histidines, to a total of seven ligands to the four copper ions of the site

distorted: At a short Cu–Cu distance of 2.47 Å (compared to 2.5 Å in the earlier analysis with synchrotron data at 2.4 Å resolution [14]), the Cu_{A2}–Sγ-C614 distance was extended to 2.6 Å, and the Cu_{A1}–Sγ-C618 distance was slightly elongated to 2.37 Å. This conformation is more similar to all other reported Cu_A sites except for *P. stutzeri*. Cu_{A1} had a nearly ideally tetrahedral ligand field with three sulfurs and a nitrogen, and all bond distances between 2.27 Å and 2.46 Å (Fig. 2E). The latter distance to the S_δ of M625 was far shorter than for typical methionine ligands in type I copper centers [49, 50]. In contrast, the geometry of Cu_{A2} diverged farther from an ideal tetrahedron, with the metal residing almost exactly in the plane of ligands C614, C618, and W616 (Fig. 2E), implying that it is better described as trigonal pyramidal. Interestingly, the second longest bond distance after the one to C618 was 2.51 Å to the backbone carbonyl of W616, suggesting a rather weak Cu–O bond. When in protomer B residue H579 rotated into the OUT-conformation (Fig. 2F), the resulting geometrical distortion of the Cu_2S_2 core was quite significant (Fig. 2G). With slight changes in distances and angles, the rhomb became more asymmetric, and the Cu_{A2}–Sγ-C614 bond weakened further, its length increasing to 2.83 Å. The Cu–Cu distance

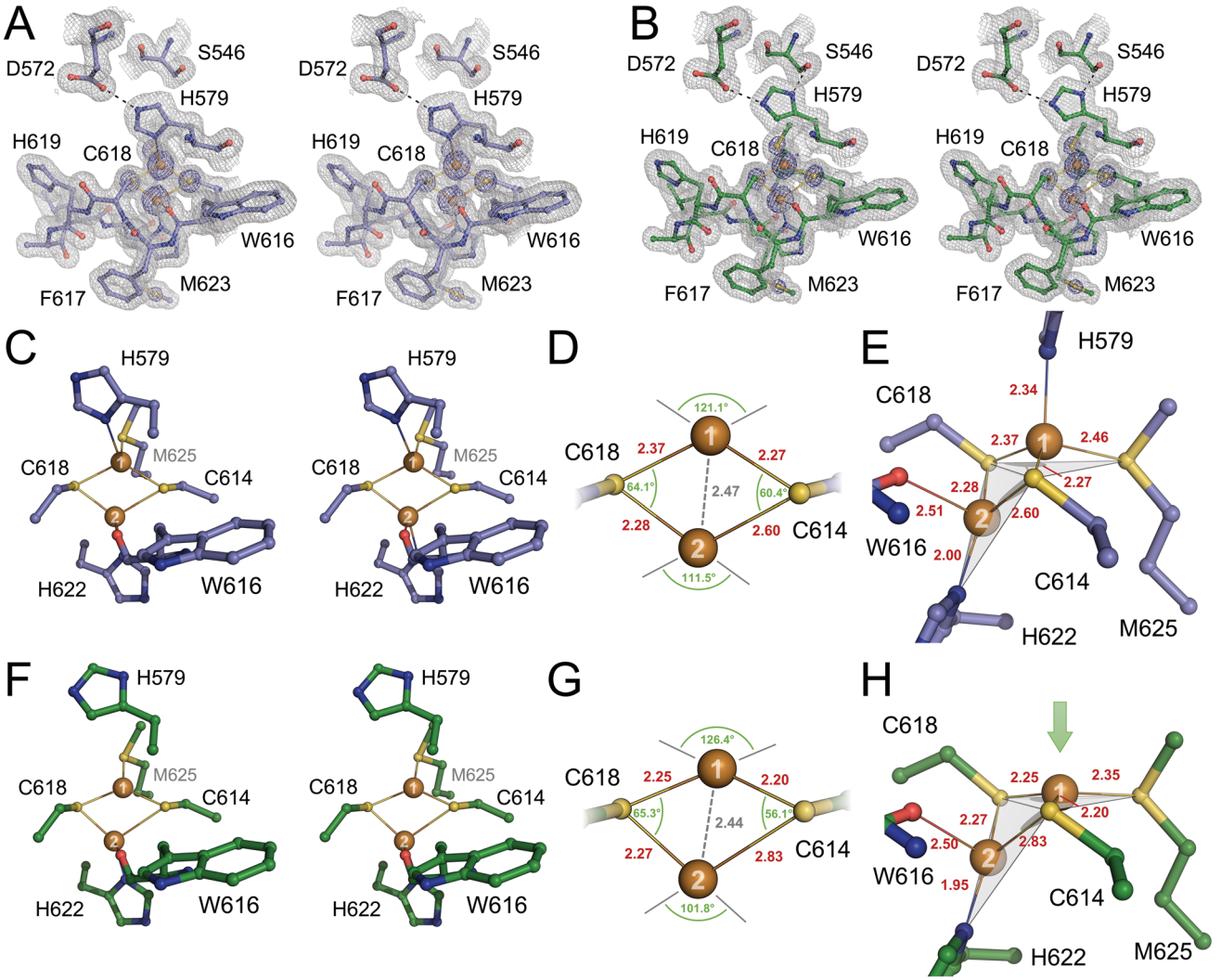

Fig. 2 The Cu_A site in *Mn*N_2OR. **A** $2F_o$–F_c difference electron density map around the Cu_A site in protomer A, contoured at the 1σ (grey) and 5σ (blue) levels. Orientation as in (**C**). **B** The corresponding representation for the Cu_A site in protomer B. **C** Cu_A in protomer A in the IN conformation of H579 with the ligands of the first coordination sphere. **D** Bond distances (in Å) and angles in the 2Cu:2S diamond core of Cu_A in protomer A, showing distortion from an ideal geometry, in particular in a long bond from Cu_{A2} to the S_γ atom of C614. **E** Contrary to [2Fe:2S] clusters, the ligand field of the copper ions is not very close to tetrahedral. While Cu_{A1} remains largely tetrahedral, with an extended bond to M625, the environment of Cu_{A2} is better described as trigonal pyramidal, with the backbone carbonyl of Q616 as an axial ligand and the Cu ion in the plane of the other three, C614, C618, and H622. **F** Cu_A with H579 in the OUT-conformation in protomer B, rendering Cu_{A1} three-coordinate. **G** The 2Cu:2S core now shows much stronger distortion, with the Cu_{A2}–C614-S_γ bond elongated to 2.83 Å. **H** With the release of H579, Cu_{A2} moves almost fully into the plane of the remaining ligands, leading to a trigonal planar coordination environment. Cu_{A2} remains largely unchanged. Panels (**A**), (**B**), (**C**), and (**F**) are rendered for wall-eyed stereo viewing

contracted only slightly to 2.44 Å. The most obvious difference, however, was geometric. While the environment of Cu_{A2} changed only with respect to C618, the missing H579 now caused Cu_{A1} to move almost fully into the plane of C614, C618, and M625, so that the coordination geometry became trigonal planar, while the environment of Cu_{A2} remained trigonal pyramidal (Fig. 2H). For *Ps*N_2OR, we previously suggested that H579 serves as a gatekeeper for electron and proton transfer in the enzyme [25, 51, 52], and the distortions of Cu_A observed here very likely also reflect in distinct changes of the midpoint potential of the site. Furthermore, the methionine ligand to Cu_{A1} was frequently designated as a weak axial ligand at this position, and the influence of the protein matrix was suggested to keep it bound, while at the same time lowering the midpoint redox potential [53]. More recently, an NMR analysis revealed significant spin density on the methionine, in line with a stronger binding and an involvement in electron transfer [54]. The present analysis adds an additional level of complexity to the electronic properties of Cu_A, in that

the methionine ligand to Cu_{A1} remains bound to the metal in both states but undergoes changes both in bond length and geometry.

Cu_Z is a [4Cu:2S] cluster

Adjacent to Cu_A but in the other protomer of the N_2OR dimer, Cu_Z is located at the hub of the N-terminal seven-bladed β-propeller domain, coordinated by seven histidine ligands: H132, H133, H181, H323, H378, H429, and H490. The fourth propeller blade that also contains the Ca^{2+}-binding loop (vide infra) is the only one that does not contribute a ligand to Cu_Z, while the second blade provides two. The first blade also provides a histidine, although its innermost β-strand is contributed by the C-terminus of the domain (Fig. 1D). Contrary to the IN- and OUT-conformations of the Cu_A sites, the four individual observations of Cu_Z were indistinguishable in the low-dose structure,

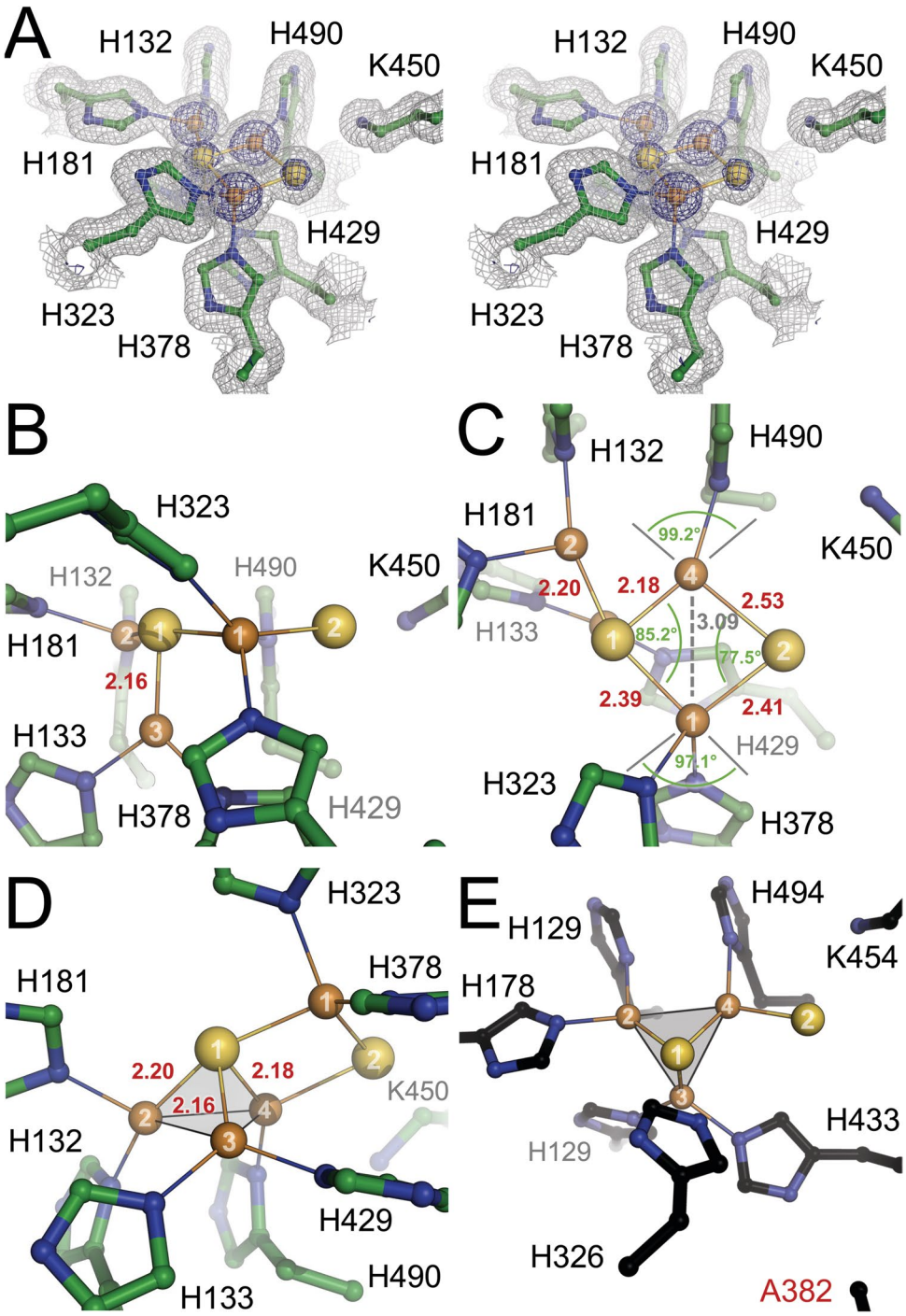

Fig. 3 The [4Cu:2S] Cu_Z site in MnN_2OR. **A** Stereo image of a $2F_o$-F_c difference electron density map around the Cu_Z site in protomer B, contoured at the 1σ (grey) and 5σ (blue) levels. **B** Front view of Cu_Z, highlighting the plane formed by Cu_{Z1}, Cu_{Z2}, Cu_{Z4} and the two sulfides. **C** Top view of Cu_Z, showing the Cu_2S_2 rhomb of Cu_{Z1} and Cu_{Z4} and the two sulfides, with distances in Å an angles. **D** Sulfide S_{Z1} coordinates all four copper ions. It forms a tetrahedron with short bond distances to Cu_{Z1}, Cu_{Z2}, and Cu_{Z3}, with short Cu–Cu distances indicative of metal–metal bonding. **E** In an H382A variant of PsN_2OR, the removal of histidine 382 led to the loss of Cu_{Z1}. The remainder of Cu_Z, with the now dangling S_{Z2} and the Cu_3S tetrahedron remained largely unchanged [27]

where Cu_Z consistently was a [4Cu: 2S] site, with a largely symmetric Cu_2S_2 diamond core that is reminiscent of Cu_A (Fig. 3A). With four metal ions, two sulfides, and seven histidine ligands, Cu_Z is a uniquely asymmetrical metal site, and the architectures reported in previous structure determinations varied substantially, in particular with respect to the Cu_{Z1}–Cu_{Z4} edge of the cluster [51]. In the present structure, Cu_Z seemed unperturbed, which was also reflected in a perfect alignment of all seven histidines with the coordinated coppers, which was not always the case in previous structures (Fig. 3A). Five of the six ions of Cu_Z were almost perfectly in a plane, with only Cu_{Z3} outside at 2.16 Å distance (Fig. 3B). Each Cu ion was liganded by two histidines, with the exception of Cu_{Z4}, to which H490 was the only protein ligand (Fig. 3B,C). The Cu_2S_2 rhomb in Cu_Z is formed by Cu_{Z1}, Cu_{Z4} and the two sulfides S_{Z1} and S_{Z2}. The Cu–S bonds to S_{Z1} were shorter than those to S_{Z2}, and the Cu_{Z1}–Cu_{Z4} distance of 3.1 Å was substantially longer than the metal–metal distance in Cu_A (Fig. 3C). Due to this, the angles in this rhomb were closer to orthogonal than in Cu_A. Arguably, the most unusual feature of this unique cluster is the arrangement of four Cu ions around the central sulfide S_{Z1}. Three of the metal ions, Cu_{Z2}, Cu_{Z3}, and Cu_{Z4}, form a nearly equilateral triangle that is completed to a tetrahedron by S_{Z1}, and the bond distances in this unit are remarkably short. The three copper ions had distances of 2.16 ± 0.03 Å to S_{Z1}, and the distances of 2.61 ± 0.01 Å for Cu_{Z2}–Cu_{Z4}, 2.64 ± 0.01 Å for Cu_{Z2}–Cu_{Z3}, and 2.81 ± 0.01 Å for Cu_{Z3}–Cu_{Z4} are indicative of metal–metal bonding. They fall in the range of distances also observed in Cu_A sites in other analyses, while these distances in Cu_A are shorter in the present structure (Fig. 2D, G). Notably, this tetrahedral structure was retained in a H382A variant of recombinant *Ps*N_2OR [27], although Cu_{Z1} was lost due to the removal of the histidine that corresponds to H378 in *Mn*N_2OR (Fig. 3E). In this structure, even the second sulfide S_{Z2} was still present, now as a dangling ligand with a long hydrogen bond to K545 (K450 in *Mn*N_2OR). It may well be the stability of this tetrahedral core that allows for the flexibility of sulfide S_{Z2}, as observed in previous analyses.

In the synchrotron data structure of *Mn*N_2OR, the position of sulfide S_{Z2} was modeled as a water molecule bridging Cu_{Z1} and Cu_{Z4} [14, 15]. However, the position of this ligand coincided very well with S_{Z2}, and the six observations of Cu_Z in the asymmetric unit of these crystals yield bond distances of 2.7 ± 0.2 Å to Cu_{Z1} and 2.3 ± 0.1 Å to Cu_{Z4} (stating only a single decimal at 2.4 Å resolution). These values agree with the Cu–S_{Z2} distances in the present analysis (Fig. 3C), but are longer than typical water ligands to copper in the range of 1.9–2.1 Å. A structurally flexible or partly occupied S_{Z2} could have been interpreted as a bridging water at moderate resolution and without additional information from anomalous scattering.

Further ion-binding sites in N_2O reductase

All known structures of N_2O reductases contain additional ion-binding sites beside the copper centers Cu_A and Cu_Z. Contrary to many other observations of surface-bound ions, these are specific sites, buried within the protein, and likely of functional importance. Although we only used diffraction data collected at a single energy, its high quality allowed us to evaluate the distinct anomalous scattering contribution of individual atoms as a means of identification. According to the Sasaki tables for anomalous scattering, the anomalous contribution of Ca^{2+} at the Cu K_α energy (8014 eV) is 1.29 e^-, while that of K^+ is 1.08 e^- [55], and there is a similar difference in the scattering contribution for Cl^- and S^{2-} (Fig. 4A). Note that all these ions are isoelectronic and therefore virtually indistinguishable in common difference electron density maps. The anomalous scattering signal is notoriously weak, but high data accuracy and a crystal form with four independent observations of each ion-binding site in the two dimers of the asymmetric unit allowed for a reliable evaluation according to the tabled values. For all sites, the refined B-factors agreed with their surroundings, indicating full occupancy (Fig. 4A).

The first site in the enzyme is a Ca^{2+} ion bound in the N-terminal β-propeller domain, connecting β-strands 2 and 3 of the fourth blade (Figs. 1D, 4B). With bound Ca^{2+}, the loop contacts the C-terminal cupredoxin domain of the other monomer, stabilizing its interaction with the β-propeller, while in an apo-structure of *Shewanella denitrificans* N_2OR, the loop was disordered in the absence of the cation [56]. Ca^{2+} binding raised the T_m of the protein, suggesting that this binding event occurs after the insertion of the copper sites to provide stability to the mature enzyme [56]. Interestingly, a recent structure of apo-N_2OR bound to the copper site maturation complex NosDFY already had Ca^{2+} bound, although both copper centers were absent [57]. However, this structure was only obtained with an inactive E154Q variant of the ABC protein NosF that rendered the complex incompetent for copper uptake and transfer to N_2OR. In the present analysis of *Mn*N_2OR, the Ca^{2+} site was fully defined and showed a typical coordination environment that in essence was octahedral but included two bidentate ligands, E260 and D274. Further ligands to Ca^{2+} were the amide oxygen of N321, the backbone amide oxygens of residues Y257 and T268, and a water molecule (Fig. 4B).

In the initial structural models for N_2OR from *P. denitrificans* and *M. nauticus*, a further ion-binding site was modeled as a second Ca^{2+} [14, 15, 17, 18]. This was contested in the analysis of *Ps*N_2OR, where the conserved feature was interpreted as a coordinated K^+ ion [25]. As calcium and potassium ions are not readily discriminated in an electron density map, the point of distinction made was the coordination environment that is the exact same in

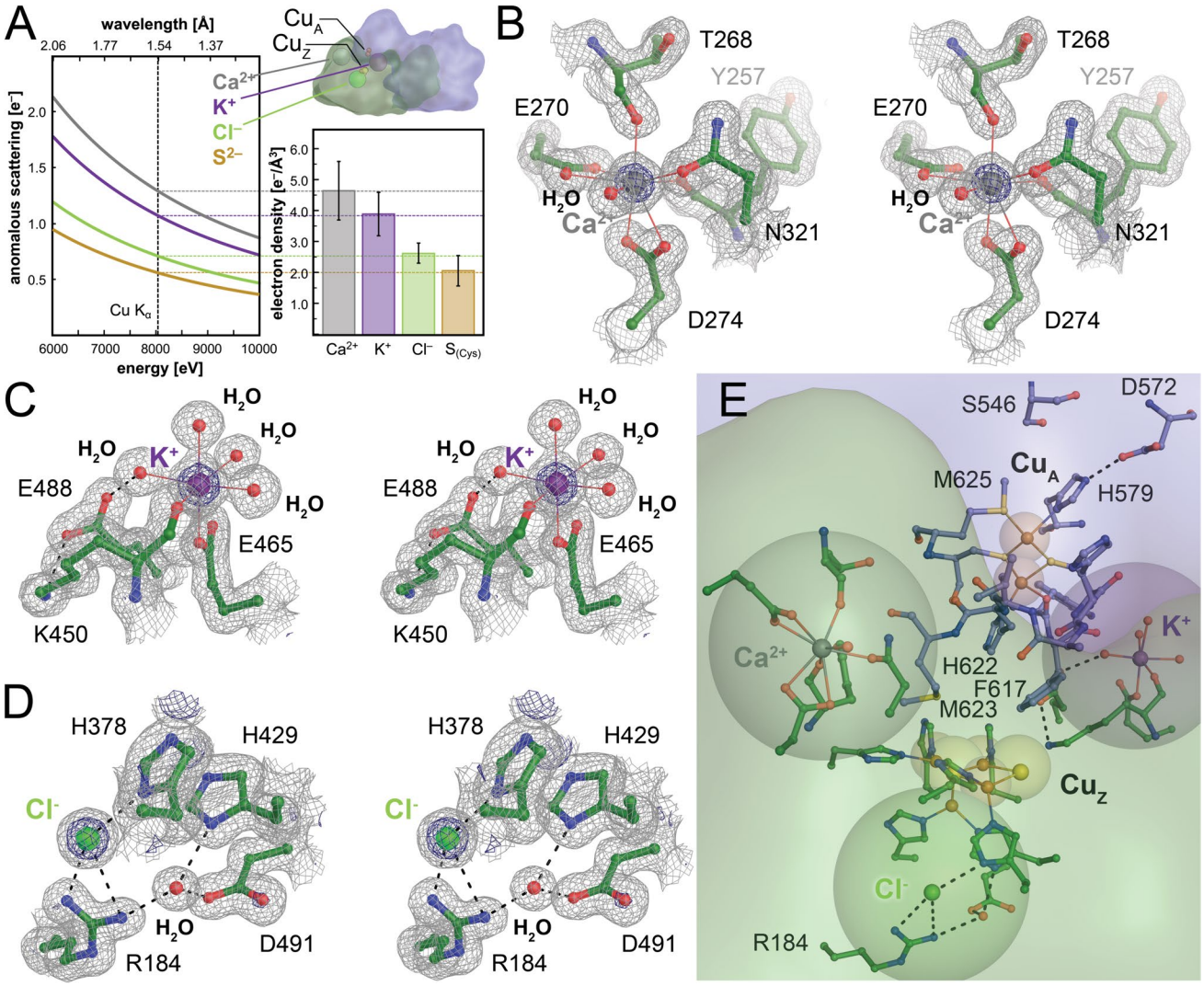

Fig. 4 Additional ion-binding sites in *Mn*N_2OR. **A** With the same number of electrons, Ca^{2+}, K^+, Cl^-, and S^{2-} cannot be distinguished in $2F_o$–F_c difference electron density maps, but their anomalous scattering contribution at Cu K_α energy differs slightly (left). The integrated anomalous difference density of the ion positions (right) scales very well with these expected differences. The depicted N_2OR dimer highlights the positions of the ions and corresponds to panel (**E**). **B** Stereo representation of the Ca^{2+} site in the β-propeller domain, with the typical bidentate coordination by two carboxylate ligands. **C** Stereo rendering of the K^+ site. The octahedral ligand field includes four waters, but only one carboxylate oxygen. **D** Stereo image of the Cl^--binding site located directly adjacent to Cu_Z [see (**E**)]. R184 as a positively charged ligands supports the assignment as an anion. All electron density maps are $2F_o$-F_c difference maps contoured at the 1σ (grey) and 5σ (blue) levels. **E** The relative positions of the ion sites with respect to the Cu_A and Cu_Z sites. Note that the K^+ ion is placed in the dimer interface, while Ca^{2+} stabilizes a loop that clamps the β-propeller domain of protomer A to the cupredoxin domain of protomer B [56]

the present structure, showing a nearly undistorted octahedral geometry. Four of the six ligands to the ion were water molecules, and only one acidic residue, E465, acted as a monodentate ligand, compensating the charge of K^+. The sixth ligand was the backbone carbonyl of the highly conserved K450, whose N_ζ amino group is close to Cu_Z. It was suggested to play a functional role during catalysis, as a proton donor for the reaction [58–60] and in supporting conformational flexibility of the Cu_Z site [27] (Fig. 4C). The integrated anomalous scattering contribution for the Ca^{2+} sites exceeded that for K^+ by exactly the expected amount (Fig. 4A). Together with the finding that upon Ca^{2+} reconstitution of the otherwise similar *S. denitrificans* N_2OR, only one site is occupied by the divalent cation [56], we conclude that this site, as in *Ps*N_2OR [25], binds K^+ specifically. The K^+ site is located on the surface of the Cu_Z domain, in the interface with the Cu_A domain of the other N_2OR protomer (Fig. 4E). Although four of its ligands are water molecules, these are buried within the protein matrix of the dimer, stabilized by a tight hydrogen-bonding network and thus not

readily exchangeable. The K^+ site furthermore is in close (if indirect) contact with Cu_A, via hydrogen bonds from water ligands, on one hand to the $N_{\varepsilon 1}$ atom of the side chain of W616 that coordinates Cu_A through its backbone carbonyl, and on the other hand to the backbone carbonyl of F617, a conserved residue that together with M623 controls access to the N_2O binding site on Cu_Z [25]. A conserved and possibly functionally essential residue is E488 that forms a hydrogen bond to a water ligand of K^+, but also to the backbone amide of F617. It also forms a salt bridge to the side chain of K450, orienting it near Cu_Z and providing a compensating charge (Fig. 4E). Taken together, F617, E488, and K450 form an efficient electron conduit between the Cu_A and the Cu_Z site. Alternatively, we have suggested that the exact same arrangement in *Ps*N_2OR (residues F621, E492, and K454) acts as a proton conduit that runs along the Cu_A site and is gated by the conformational change of the distal histidine ligand to Cu_A, H579 [52]. The present analysis of the *Mn*N_2OR structure is fully in line with this. The second ion-binding site in N_2OR thus holds a K^+ ion that plays a very specific role in connecting the Cu_A and Cu_Z sites, integrating them into a single functional active site within N_2OR. For N_2OR assembly, this choice of ions is deliberate. Calcium binding locks the structure in a closed state that no longer allows for the insertion of copper during the maturation of the enzyme in the periplasm [56], while the position of K^+ indicates that it already is inserted upon dimerization of apo-NosZ. This step occurs in the cytoplasm prior to the export of the enzyme as a folded dimer via the Tat system, and the K^+ site is no longer accessible after the dimer has formed [56]. It is, therefore, important that the correct ion binds in the proper sequence in the right cellular compartment.

One additional ion-binding site was consistently observed in all structures of N_2OR enzymes reported to date. Located close to the Cu_Z site, a significant electron density peak appeared that could not be modeled as water. Due to its position close to the positively charged R184 (*M. nauticus* numbering) and an electron density peak with approximately twice the magnitude of a water (after occupancy refinement), this feature was modeled as a chloride anion. Besides R184, the only other amino acid that directly ligated this ion was H378, a ligand to Cu_{Z1} (Fig. 4D). The role of this ion is unclear, although its charge may help in shaping the electrostatic environment of the Cu_Z site. Moreover, chloride is not easy to distinguish from the isoelectronic hydrosulfide anion, HS^-, adding to the enigma of the possible flexibility of S_{Z2}, as discussed above. The average anomalous signal peak intensity at this position is slightly higher than that for all cysteine sulfides in the structure, but as the varying *B*-factors of these amino acids in different parts of the structure play strongly into this measurement and the anomalous signal strength for chloride should only be 14% higher than for sulfide, the distinction is not a clear as for the case of K^+ versus Ca^{2+}. We therefore used only the most well-defined sulfur atoms in the structure, the cysteine S_γ atoms, but not the S_δ of methionines. Here, the sulfur anomalous signal perfectly coincided with the tabled values, while the four presumed Cl^- sites showed a stronger signal that corresponded to the Sasaki values for this element (Fig. 4A). Our analysis of the anomalous scattering properties of all ion sites supports an assignment as Cl^- rather than S^{2-}, but its influence on the properties of Cu_Z—if any—remains to be understood.

Implications for the catalytic mechanism of N_2OR

The electron-transferring Cu_A and the unique Cu_Z combine at a dimer interface to create an intricate active site for the reduction of inert N_2O. The observation of two distinct conformations of Cu_A in the present analysis is in line with our earlier findings on *Ps*N_2OR [25, 26], but it has not been reported for any of the multiple other descriptions of mixed-valent Cu_A sites. Most intriguingly, the precise definition of two conformations for Cu_A implies that the C_2-symmetric N_2OR dimer must pack in the crystal lattice in a non-random fashion, as otherwise the two conformations of the site should be randomly distributed, and the resulting electron density maps should represent an average of both conformations. We initially assumed that the IN- and OUT-conformations of Cu_A might lead to changes at the protein surface that could then affect crystal packing, but we could not identify any significant differences between the two protomers. Both the *P. stutzeri* and the present *M. nauticus* enzyme crystallized in the lowest-symmetry space group, triclinic *P*1, resulting in a rather simple crystal packing that may prevent that different conformations average out, so that it remains possible that this feature could not be discerned in other structures. Note also that the serine required for the OUT-conformation (S546 in *Mn*N_2OR) is conserved in N_2OR sequences, but not in the Cu_A domains of oxidases or the engineered sites in generic cupredoxins. Mechanistically, a gating mechanism for electron transfer to and through Cu_A is highly interesting. Cu_A is a single-electron transfer site, so that the 2-electron reduction of N_2O to N_2 should proceed in two consecutive reduction steps, possibly with an enzyme-bound intermediate, formally $[N_2O]^-$. In this case, the role of Cu_Z would be to bind and activate N_2O as a prerequisite for electron transfer from Cu_A. The finding that crystals of N_2OR bind N_2O between the Cu_Z and Cu_A sites upon pressurization with the gas is well in line with this model [25]. However, we so far failed to isolate and analyze a one-electron-reduced intermediate of the reaction, which should be formed if enzyme with reduced Cu_A was incubated with N_2O in the absence of further reductant. In addition, N_2OR exhibited higher catalytic activity when Cu_Z was reduced to an all-cuprous state with 4 Cu(I) [60]. Turnover from this highly reduced state led to a one-electron-oxidized form,

designated Cu_Z^0. While at the same redox level as the Cu_Z* state, only Cu_Z^0 could be reduced from Cu_A using a physiological reductant [60]. The mechanistic implication is that for the reduction of N_2O, one electron is provided by Cu_Z and the other by Cu_A. This results in a concerted 2-electron reduction, presumably without a long-lived intermediate. The observed transition from an OUT to an IN conformation upon N_2O binding [25] may be key to this process, as the geometric changes reported here likely affect the midpoint potential for Cu_A and potentially serve as a trigger for electron transfer to the substrate.

The observed uniformity of the unique Cu_Z cluster indicates that the heterogeneity seen before at this site may indeed have been due to radiation damage or photoreduction processes during data collection. Available structures mostly differ in the ligand or ligands bridging Cu_{Z1} and Cu_{Z4}, but not in the tetrahedral core formed by Cu_{Z2-4} and S_{Z1}. Previously, this was interpreted as lability of S_{Z2} that was postulated to fully dissociate from the cluster to facilitate N_2O binding as a bridging ligand to Cu_{Z1} and Cu_{Z4} [29, 61]. The H382A variant of *Ps*N_2OR then revealed that the spectroscopic differences between form I and II of the enzyme, or the Cu_Z and Cu_Z* form of the active site cluster, are also reproduced if S_{Z2} dissociates only from Cu_{Z1} to interact with the nearby lysine [27]. This flexibility can rationalize that S_{Z2} in many structures seems to have lower electron density (leading to an assignment as OH^-) or even two distinct positions that were then interpreted as bound water. Further work will be required to confirm this hypothesis and deliberately populate the two conformational states for in-depth analysis. Also, in many cases, one or several of the histidine ligands to the copper ions are not ideally oriented toward the metal, indicating that the observed structures may be partially demetallated. This is another typical effect of radiation damage, and the structural uniformity of Cu_Z in the present analysis at low X-ray dose underscores the value of this approach for the analysis of sensitive metal sites in general and the intrinsically flexible Cu_Z in particular.

Acknowledgements This work was supported by the Deutsche Forschungsgemeinschaft (RTG 1976, Project No. 235777276, and PP 1927, Project No. 311061829 to O.E.) and the European Research Council (Grant No. 310656 to O.E.). The authors thank Lin Zhang for the helpful discussions. This work was also supported by national funds from Fundação para a Ciência e Tecnologia (FCT) under the scope of the project UIDP/04378/2020 and UIDB/04378/2020 of the Research Unit on Applied Molecular Biosciences—UCIBIO, the project LA/P/0140/2020 of the Associate Laboratory Institute for Health and Bioeconomy—i4HB, and the projects UIDB/50006/2020 and UIDP/50006/2020 of the Laboratório Associado de Química Verde–LAQV. FCT has also supported I.M. through the project 2022.01152.PTDC, and S.D. was supported by an EMBO Short-Term Fellowship (ref. ASTF 282.00-2010).

Funding Open Access funding enabled and organized by Projekt DEAL. This work was funded by European Molecular Biology Organization, ASTF 282.00-2010, Deutsche Forschungsgemeinschaft, PP 1927, Project No. 311061829, RTG 1976, Project No. 235777276, FP7 Ideas: European Research Council, 310656, Fundação para a Ciência e a Tecnologia, 2022.01152.PTDC, UCIBIO, the project LA/P/0140/2020, UIDB/50006/2020, and UIDP/50006/2020.

Data availability The atomic coordinates and experimental structure factor amplitudes for the low-dose structure of *M. nauticus* N_2OR have been deposited with the Protein Data Bank at http://www.pdb.org with the accession number 9F8X.

Declarations

Conflict of interest The authors declare no conflict of interest.

References

1. Zumft WG (1997) Microbiol Mol Biol Rev 61:533–616
2. Einsle O, Kroneck PMH (2004) Biol Chem 385:875–883
3. Pauleta SR, Dell'Acqua S, Moura I (2013) Coord Chem Rev 257:332–349
4. Wüst A, Schneider L, Pomowski A, Zumft WG, Kroneck PMH, Einsle O (2012) Biol Chem 393:1067–1077
5. Zumft WG, Kroneck PMH (2007) Adv Microb Physiol 52:107–225
6. Canfield DE, Glazer AN, Falkowski PG (2010) Science 330:192–196
7. Schmittner A, Galbraith ED (2008) Nature 456:373–376
8. Ravishankara AR, Daniel JS, Portmann RW (2009) Science 326:123–125
9. Sproer C, Lang E, Hobeck P, Burghardt J, Stackebrandt E, Tindall BJ (1998) Int J Syst Bacteriol 48:1445–1448
10. Gauthier MJ, Lafay B, Christen R, Fernandez L, Acquaviva M, Bonin P, Bertrand JC (1992) Int J Syst Bacteriol 42:568–576
11. Prudêncio M, Pereira AS, Tavares P, Besson S, Moura I (1999) J Inorg Biochem 74:267–267
12. Carreira C, dos Santos MMC, Pauleta SR, Moura I (2020) Bioelectrochemistry 133:107483
13. Iwata S, Ostermeier C, Ludwig B, Michel H (1995) Nature 376:660–669
14. Brown K, Tegoni M, Prudêncio M, Pereira AS, Besson S, Moura JJ, Moura I, Cambillau C (2000) Nat Struct Biol 7:191–195
15. Brown K, Djinovic-Carugo K, Haltia T, Cabrito I, Saraste M, Moura JJG, Moura I, Tegoni M, Cambillau C (2000) J Biol Chem 275:41133–41136
16. Prudêncio M, Pereira AS, Tavares P, Besson S, Cabrito I, Brown K, Samyn B, Devreese B, Van Beeumen J, Rusnak F, Fauque G, Moura JJG, Tegoni M, Cambillau C, Moura I (2000) Biochemistry 39:3899–3907

17. Haltia T, Brown K, Tegoni M, Cambillau C, Saraste M, Mattila K, Djinovic-Carugo K (2003) Biochem J 369:77–88
18. Paraskevopoulos K, Antonyuk SV, Sawers RG, Eady RR, Hasnain SS (2006) J Mol Biol 362:55–65
19. Solomon EI, Heppner DE, Johnston EM, Ginsbach JW, Cirera J, Qayyum M, Kieber-Emmons MT, Kjaergaard CH, Hadt RG, Tian L (2014) Chem Rev 114:3659–3853
20. Dell'Acqua S, Pauleta SR, Moura I, Moura JJG (2011) J Biol Inorg Chem 16:183–194
21. Riester J, Zumft WG, Kroneck PMH (1989) Eur J Biochem 178:751–762
22. Fujita K, Chan JM, Bollinger JA, Alvarez ML, Dooley DM (2007) J Inorg Biochem 101:1836–1844
23. Dell'Acqua S, Pauleta SR, Moura JJ, Moura I (2012) Philos Trans R Soc Lond B Biol Sci 367:1204–1212
24. Pomowski A, Zumft WG, Kroneck PMH, Einsle O (2010) Acta Crystallogr Sect F Cryst Comm 66:1541–1543
25. Pomowski A, Zumft WG, Kroneck PMH, Einsle O (2011) Nature 477:234–237
26. Zhang L, Wüst A, Prasser B, Müller C, Einsle O (2019) Proc Natl Acad Sci USA 116:12822–12827
27. Zhang L, Bill E, Kroneck PMH, Einsle O (2021) Chem Sci 12:3239–3244
28. Johnston EM, Dell'Acqua S, Pauleta SR, Moura I, Solomon EI (2015) Chem Sci 6:5670–5679
29. Ghosh S, Gorelsky SI, Chen P, Cabrito I, Moura JJG, Moura I, Solomon EI (2003) J Am Chem Soc 125:15708–15709
30. Gorelsky SI, Ghosh S, Solomon EI (2006) J Am Chem Soc 128:278–290
31. Johnston EM, Dell'Acqua S, Ramos S, Pauleta SR, Moura I, Solomon EI (2014) J Am Chem Soc 136:614–617
32. Smith PK, Krohn RI, Hermanson GT, Mallia AK, Gartner FH, Provenzano MD, Fujimoto EK, Goeke NM, Olson BJ, Klenk DC (1985) Anal Biochem 150:76–85
33. Kabsch W (2010) Acta Crystallogr Sect D 66:125–132
34. Evans PR, Murshudov GN (2013) Acta Crystallogr Sect D 69:1204–1214
35. Winn MD, Ballard CC, Cowtan KD, Dodson EJ, Emsley P, Evans PR, Keegan RM, Krissinel EB, Leslie AGW, McCoy A, McNicholas SJ, Murshudov GN, Pannu NS, Potterton EA, Powell HR, Read RJ, Vagin A, Wilson KS (2011) Acta Crystallogr Sect D 67:235–242
36. Vagin A, Teplyakov A (2010) Acta Crystallogr Sect D 66:22–25
37. Emsley P, Lohkamp B, Scott WG, Cowtan K (2010) Acta Crystallogr D Biol Crystallogr 66:486–501
38. Murshudov GN, Skubak P, Lebedev AA, Pannu NS, Steiner RA, Nicholls RA, Winn MD, Long F, Vagin AA (2011) Acta Crystallogr D Biol Crystallogr 67:355–367
39. Chen VB, Arendall WB 3rd, Headd JJ, Keedy DA, Immormino RM, Kapral GJ, Murray LW, Richardson JS, Richardson DC (2010) Acta Crystallogr D Biol Crystallogr 66:12–21
40. Beinert H (1988) Ann N Y Acad Sci 550:374–379
41. Beinert H (1997) Eur J Biochem 245:521–532
42. Kroneck PMH, Antholine WA, Riester J, Zumft WG (1989) FEBS Lett 248:212–213
43. Li PM, Malmström BG, Chan SI (1989) FEBS Lett 248:210–211
44. Kroneck PMH, Antholine WE, Kastrau DHW, Buse G, Steffens GCM, Zumft WG (1990) FEBS Lett 268:274–276
45. Farrar JA, Neese F, Lappalainen P, Kroneck PMH, Saraste M, Zumft WG, Thomson AJ (1996) J Am Chem Soc 118:11501–11514
46. Kroneck PMH (2018) J Biol Inorg Chem 23:27–39
47. Williams PA, Blackburn NJ, Sanders D, Bellamy H, Stura EA, Fee JA, McRee DE (1999) Nat Struct Biol 6:509–516
48. Liu J, Chakraborty S, Hosseinzadeh P, Yu Y, Tian SL, Petrik I, Bhagi A, Lu Y (2014) Chem Rev 114:4366–4469
49. Hwang HJ, Berry SM, Nilges MJ, Lu Y (2005) J Am Chem Soc 127:7274–7275
50. Karlsson BG, Nordling M, Pascher T, Tsai LC, Sjolin L, Lundberg LG (1991) Protein Eng 4:343–349
51. Schneider LK, Wüst A, Pomowski A, Zhang L, Einsle O (2014) Metal Ions Life Sci 14:177–210
52. Zhang L, Bill E, Kroneck PMH, Einsle O (2021) J Am Chem Soc 143:830–838
53. Tsai ML, Hadt RG, Marshall NM, Wilson TD, Lu Y, Solomon EI (2013) Proc Natl Acad Sci USA 110:14658–14663
54. Morgada MN, Llases ME, Giannini E, Castro MA, Alzari PM, Murgida DH, Lisa MN, Vila AJ (2020) Chem Commun (Camb) 56:1223–1226
55. Sasaki S (1989) KEK Report. National Laboratory for High-Energy Physics, Ibaraki, Japan
56. Schneider LK, Einsle O (2016) Biochemistry 55:1433–1440
57. Müller C, Zhang L, Zipfel S, Topitsch A, Lutz M, Eckert J, Prasser B, Chami M, Lü W, Du J, Einsle O (2022) Nature 608:626–631
58. Ghosh S, Gorelsky SI, George SD, Chan JM, Cabrito I, Dooley DM, Moura JJG, Moura I, Solomon EI (2007) J Am Chem Soc 129:3955–3965
59. Bagherzadeh S, Mankad NP (2018) Chem Commun 54:1097–1100
60. Johnston EM, Carreira C, Dell'Acqua S, Dey SG, Pauleta SR, Moura I, Solomon EI (2017) J Am Chem Soc 139:4462–4476
61. Chen P, Gorelsky SI, Ghosh S, Solomon EI (2004) Angew Chem Int Edit 43:4132–4140
62. Weiss M, Hilgenfeld R (1997) J Appl Crystallogr 30:203–205
63. Karplus PA, Diederichs K (2012) Science 336:1030–1033
64. Cruickshank DWJ (1999) Acta Crystallogr Sect D 55:583–601
65. Laskowski RA, MacArthur MW, Moss DS, Thornton JM (1993) J Appl Crystallogr 26:283–291